The Astronomical Journal, 163:133 (15pp), 2022 March https://doi.org/10.3847/1538-3881/ac4af0

A Transiting, Temperate Mini-Neptune Orbiting the M Dwarf TOI-1759 Unveiled by TESS

Néstor Espinoza[1], Enric Pallé[2], Jonas Kemmer[3], Rafael Luque[4], José A. Caballero[5], Carlos Cifuentes[5], Enrique Herrero[6,7], Víctor J. Sánchez Béjar[2,8], Stephan Stock[3], Karan Molaverdikhani[3,9,10,11], Giuseppe Morello[2,8], Diana Kossakowski[9], Martin Schlecker[9], Pedro J. Amado[4], Paz Bluhm[3], Miriam Cortés-Contreras[5], Thomas Henning[9], Laura Kreidberg[9], Martin Kürster[9], Marina Lafarga[6,7], Nicolas Lodieu[2,8], Juan Carlos Morales[6,7], Mahmoudreza Oshagh[2,8], Vera M. Passegger[12,13], Alexey Pavlov[9], Andreas Quirrenbach[3], Sabine Reffert[3], Ansgar Reiners[14], Ignasi Ribas[6,7], Eloy Rodríguez[4], Cristina Rodríguez López[4], Andreas Schweitzer[13], Trifon Trifonov[9], Priyanka Chaturvedi[15], Stefan Dreizler[14], Sandra V. Jeffers[16], Adrian Kaminski[3], María José López-González[4], Jorge Lillo-Box[5], David Montes[17], Grzegorz Nowak[2,8], Santos Pedraz[18], Siegfried Vanaverbeke[19,20], Maria R. Zapatero Osorio[21], Mathias Zechmeister[14], Karen A. Collins[22], Eric Girardin[23], Pere Guerra[24], Ramon Naves[24], Ian J. M. Crossfield[25], Elisabeth C. Matthews[26], Steve B. Howell[27], David R. Ciardi[28], Erica Gonzales[29], Rachel A. Matson[30], Charles A. Beichman[28], Joshua E. Schlieder[31], Thomas Barclay[31,32], Michael Vezie[33], Jesus Noel Villaseñor[33], Tansu Daylan[33], Ismael Mireles[34], Diana Dragomir[34], Joseph D. Twicken[27,35], Jon Jenkins[27], Joshua N. Winn[36], David Latham[22], George Ricker[33], and Sara Seager[33]

[1] Space Telescope Science Institute, 3700 San Martin Drive, Baltimore, MD 21218, USA; nespinoza@stsci.edu
[2] Instituto de Astrofísica de Canarias (IAC), E-38205 La Laguna, Tenerife, Spain
[3] Landessternwarte, Zentrum für Astronomie der Universität Heidelberg, Königstuhl 12, D-69117 Heidelberg, Germany
[4] Instituto de Astrofísica de Andalucía (CSIC), Glorieta de la Astronomía s/n, E-18008 Granada, Spain
[5] Centro de Astrobiología (CSIC-INTA), ESAC, Camino bajo del castillo s/n, E-28692 Villanueva de la Cañada, Madrid, Spain
[6] Institut de Ciències de l'Espai (ICE, CSIC), Campus UAB, c/ de Can Magrans s/n, E-08193 Cerdanyola del Vallès, Barcelona, Spain
[7] Institut d'Estudis Espacials de Catalunya (IEEC), c/ Gran Capità 2–4, E-08034 Barcelona, Spain
[8] Departamento de Astrofísica, Universidad de La Laguna, E-38206 La Laguna, Tenerife, Spain
[9] Max-Planck-Institut für Astronomie, Königstuhl 17, D-69117 Heidelberg, Germany
[10] Universitäts-Sternwarte, Ludwig-Maximilians-Universität München, Scheinerstrasse 1, D-81679 München, Germany
[11] ORIGINS: Exzellenzcluster Origins, Boltzmannstrae 2, D-85748 Garching, Germany
[12] Homer L. Dodge Department of Physics and Astronomy, University of Oklahoma, 440 West Brooks Street, Norman, OK 73019, USA
[13] Hamburger Sternwarte, Gojenbergsweg 112, D-21029 Hamburg, Germany
[14] Institut für Astrophysik, Georg-August-Universität, Friedrich-Hund-Platz 1, D-37077 Göttingen, Germany
[15] Thüringer Landessternwarte Tautenburg, Sternwarte 5, D-07778 Tautenburg, Germany
[16] Max-Planck-Institute für Sonnensystemforschung, Justus-von-Liebig-Weg 3, D-37075 Göttingen, Germany
[17] Departamento de Física de la Tierra y Astrofísica & IPARCOS-UCM (Instituto de Física de Partículas y del Cosmos de la UCM), Facultad de Ciencias Físicas, Universidad Complutense de Madrid, E-28040 Madrid, Spain
[18] Centro Astronómico Hispano-Alemán, Observatorio de Calar Alto, Sierra de los Filabres, E-04550 Gérgal, Almería, Spain
[19] Vereniging Voor Sterrenkunde, Brugge & Centre for Mathematical Plasma-Astrophysics, Department of Mathematics, KU Leuven, Celestijnenlaan 200B, B-3001 Heverlee, Belgium
[20] AstroLAB IRIS, Provinciaal Domein "De Palingbeek", Verbrandemolenstraat 5, B-8902 Zillebeke, Ieper, Belgium
[21] Centro de Astrobiología (CSIC-INTA), Carretera de Ajalvir km 4, E-28850 Torrejón de Ardoz, Madrid, Spain
[22] Center for Astrophysics | Harvard & Smithsonian, 60 Garden Street, Cambridge, MA 02138, USA
[23] Grand Pra Observatory, Switzerland
[24] Observatori Astronòmic Albanyà, Camí de Bassegoda s/n, Albanyà E-17733, Girona, Spain
[25] Department of Physics and Astronomy, University of Kansas, Lawrence, KS 66045, USA
[26] Observatoire de l'Université de Genève, Chemin Pegasi 51, 1290 Versoix, Switzerland
[27] NASA Ames Research Center, Moffett Field, CA 94035, USA
[28] NASA Exoplanet Science Institute, Caltech-IPAC, MC 314-6, 1200 E California Boulevard, Pasadena, CA 91125, USA
[29] Department of Astronomy and Astrophysics, University of California, Santa Cruz, CA 95060, USA
[30] U.S. Naval Observatory, Washington, D.C. 20392, USA
[31] NASA Goddard Space Flight Center, 8800 Greenbelt Road, Greenbelt, MD 20771, USA
[32] University of Maryland, Baltimore County, 1000 Hilltop Circle, Baltimore, MD 21250, USA
[33] Department of Physics and Kavli Institute for Astrophysics and Space Research, Massachusetts Institute of Technology, Cambridge, MA 02139, USA
[34] Department of Physics and Astronomy, University of New Mexico, 210 Yale Boulevard NE, Albuquerque, NM 87106, USA
[35] SETI Institute, Mountain View, CA 94043, USA
[36] Department of Astrophysical Sciences, Princeton University, 4 Ivy Lane, Princeton, NJ 08544, USA
Received 2021 August 14; revised 2022 January 3; accepted 2022 January 5; published 2022 February 16

Abstract

We report the discovery and characterization of TOI-1759 b, a temperate (400 K) sub-Neptune-sized exoplanet orbiting the M dwarf TOI-1759 (TIC 408636441). TOI-1759 b was observed by TESS to transit in Sectors 16, 17, and 24, with only one transit observed per sector, creating an ambiguity regarding the orbital period of the planet candidate. Ground-based photometric observations, combined with radial-velocity measurements obtained with the CARMENES spectrograph, confirm an actual period of 18.85019 ± 0.00014 days. A joint analysis of all available

photometry and radial velocities reveals a radius of $3.17 \pm 0.10\,R_\oplus$ and a mass of $10.8 \pm 1.5\,M_\oplus$. Combining this with the stellar properties derived for TOI-1759 ($R_\star = 0.597 \pm 0.015\,R_\odot$; $M_\star = 0.606 \pm 0.020\,M_\odot$; $T_{\rm eff} = 4065 \pm 51$ K), we compute a transmission spectroscopic metric (TSM) value of over 80 for the planet, making it a good target for transmission spectroscopy studies. TOI-1759 b is among the top five temperate, small exoplanets ($T_{\rm eq} < 500$ K, $R_p < 4\,R_\oplus$) with the highest TSM discovered to date. Two additional signals with periods of 80 days and >200 days seem to be present in our radial velocities. While our data suggest both could arise from stellar activity, the later signal's source and periodicity are hard to pinpoint given the ∼200 days baseline of our radial-velocity campaign with CARMENES. Longer baseline radial-velocity campaigns should be performed in order to unveil the true nature of this long-period signal.

Unified Astronomy Thesaurus concepts: Exoplanet astronomy (486)

Supporting material: machine-readable tables

1. Introduction

One of the most exciting astronomical developments in the last decade, triggered by improved instrumentation and survey designs, is the detection and characterization of small ($R_p < 4\,R_\oplus$) exoplanets. The study of transiting, relatively low-temperature small worlds, in particular, promises to provide key information to understand how different environments (e.g., incident stellar fluxes or initial composition) might impact their bulk properties, and how those might in turn change their atmospheric and interior structures (Dorn et al. 2017; Neil & Rogers 2020; Ma & Ghosh 2021). In addition, these cooler worlds allow us to make connections with the planets in our own solar system, all of which have equilibrium temperatures smaller than 500 K (hereon referred to as "temperate" exoplanets). These connections, in turn, have key implications for the search for life outside the solar system, and have the potential to help us improve and refine the concept of planetary habitability itself (Tasker et al. 2017; Meadows & Barnes 2018; Seager et al. 2021).

Detecting these small, temperate exoplanets is, however, challenging. The relatively longer orbital periods needed to have small irradiation levels makes them difficult to detect from the ground using the transit technique, which is why most of the known temperate worlds were detected by the transit survey with the longest continuous time baseline: the Kepler mission (Borucki et al. 2010). While revolutionary in the search and discovery of small worlds—revealing that they are, in fact, among the most abundant population of exoplanets in our Galaxy (at least for close-in exoplanets; Fulton & Petigura 2018; Hsu et al. 2019)—the mission provided few systems amenable for further radial-velocity and/or atmospheric characterization, due to the inherent faintness of the stars it surveyed. This detailed characterization is fundamental to understand the overall makeup of these small, distant worlds, and helps us understand and uncover their different subpopulations (see, e.g., Zeng et al. 2019; Gupta & Schlichting 2021; Schlichting & Young 2021; Yu et al. 2021). It is also important to understand fundamental exoplanet demographic questions such as *why* these small worlds are the most numerous in our Galaxy (see, e.g., Kite et al. 2019).

The Transiting Exoplanet Survey Satellite (Ricker et al. 2015; TESS) has been crucial to the search for small transiting exoplanets amenable for detailed characterization. To date, it has already doubled the known sample of small, temperate worlds for which masses have been measured with follow-up observations. And after three years of operation, the mission is just starting to exploit its long-time baselines, allowing for the discovery of exoplanets on long orbital periods. In this work, we present the detection and characterization of one such system: TOI-1759 b, an 18.85 days sub-Neptune ($R_p = 3.14\,R_\oplus$, $M_p = 10.8\,M_\oplus$), orbiting a M-dwarf star.

This paper is structured as follows. In Section 2 we describe the data that were obtained to understand this new exoplanetary system, which includes photometric, spectroscopic, and high-resolution imaging data. In Section 3 we present the analysis of these data, including the stellar and planetary properties of the system. We discuss our results in Section 4, and summarize our main conclusions from this work in Section 5.

2. Observations

2.1. TESS

Observations from TESS for TOI-1759 (TYC 4266-736-1, TIC408636441) were obtained during its second year of operation in its high-cadence, 2 minutes exposure mode in Sectors 16 (2019 September to October), 17 (2019 October to November), and 24 (2020 April to May—see Figures 1 and 2; the data are also presented in Table 6).

The 2 minutes cadence data were processed in the TESS Science Processing Operations Center (SPOC; Jenkins et al. 2016) photometry and transit search pipelines (Jenkins 2002; Jenkins et al. 2010) at NASA Ames Research Center. The TESS data validation reports (Twicken et al. 2018; Li et al. 2019) on TOI-1759 (Guerrero et al. 2021) show detections of a transiting exoplanet candidate at a 37.7 days period (although the data were also consistent with a planet at half this period, i.e., 18.85 days) and a transit depth of about 2700 ppm. To perform further analyses on this target, we retrieved the Pre-Data-Conditioning (PDC)−corrected photometry (Smith et al. 2012; Stumpe et al. 2012, 2014) from all sectors from the Mikulski Archive for Space Telescopes archive[37], as this is the highest-quality photometry from the three TESS sectors mentioned above. After removing the transits of the planet candidate, we ran the Transit Least Squares (TLS; Hippke & Heller 2019) algorithm on these photometric time series and found no extra significant signals (i.e., signals with a signal-to-noise ratio >5) in the data.

2.2. CARMENES Spectroscopy

We monitored TOI-1759 with the CARMENES[38] instrument located on the 3.5 m telescope at the Calar Alto Observatory in Almería, Spain, from 2020 July 24 to 2021 January 17. Our data covered a time span of about 175 days, over which we

[37] https://archive.stsci.edu/

[38] Calar Alto high-Resolution search for M dwarfs with Exo-earths with Near-infrared and optical Échelle Spectrographs, http://carmenes.caha.es.

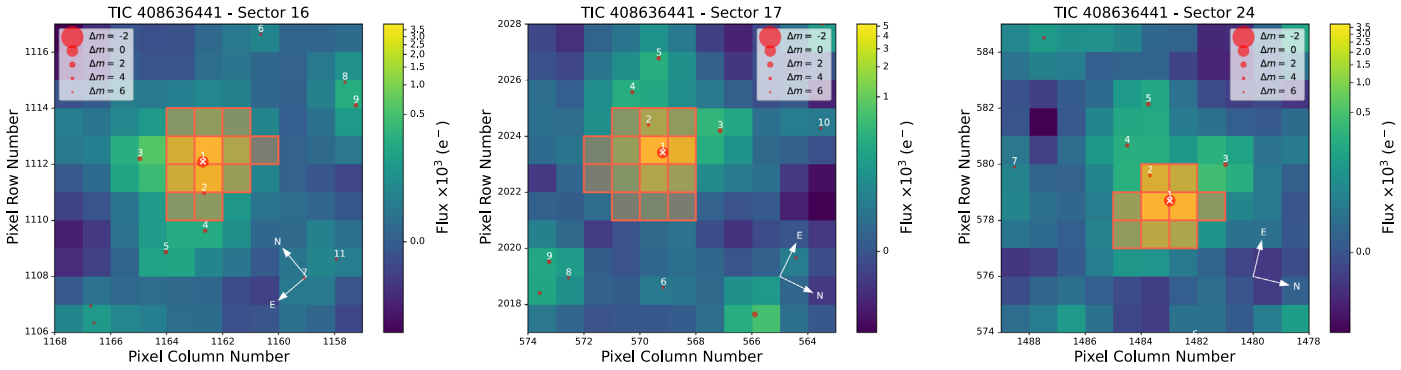

Figure 1. TESS target pixel files (TPFs) for TOI-1759 from the different sectors from which data were gathered with the mission (Sector 16, left; 17, center; 24, right). TOI-1759 is marked with a white cross on top of a red point and is numbered 1. Smaller numbered red points are the closest stars to the target (drawn from Gaia) with Gaia magnitude differences with the target of $|\Delta G| < 6$ mag. Contamination is not a problem for TOI-1759, as most nearby targets are very faint. The plot is made using `tpfplotter` (Aller et al. 2020).

were able to detect significant radial-velocity signals. The spectra were processed following the standard CARMENES data flow (Caballero et al. 2016) that has been extensively used by previous works (e.g., Zechmeister et al. 2018; Morales et al. 2019; Trifonov et al. 2020). In our analyses, we only used radial velocities from the visual (VIS) channel that had mean errors of 2.6 m s^{-1}. A total of 57 radial-velocity data points were used for our analysis, which are presented in Table 5. The spectra used to derive those have a median signal-to-noise ratio of 95 at 840 nm. Data from our infrared channel were not used, as their precision (mean error of 10 m s^{-1}) was not high enough to put meaningful constraints on the radial-velocity variations observed in the VIS channel.

Figure 3(a) shows the radial velocity as a function of time as observed through the VIS channel, which covers the spectral range 520–960 nm with a spectral resolution of $R = 94,600$ (Quirrenbach et al. 2014, 2018). Our campaign allowed us to clearly detect a signal at about 18.5 days (consistent with half the period of the transiting exoplanet detected in the TESS photometry, already discussed in Section 2.1) on top of an additional long-term radial-velocity signal. We discuss the details of our analysis of these signals in Section 3.

2.3. Ground-based Photometry

Ground-based photometric follow-up observations were performed as part of the TESS Follow-up Program's (TFOP) Subgroup 1 (SG1). Among the observations, a transit of TOI-1759 b in 2020 May 21 was captured by three independent telescopes/observatories: the OAA telescope of the Observatori Astronòmic Albanyà (Albanyà Spain; 4 hr of total observing time, per-point precision of 1140 ppm at 1 minutes cadence; R-filter observations), the RCO telescope of the Grand-Pra Observatory (Valais Sion, Switzerland; 6 hr of total observing time, per-point precision of 1080 ppm at 1.3 minutes cadence; i_p-filter observations), and the OMC telescope of the Montcabrer Observatory (Barcelona, Spain; 5 hr of total observing time, per-point precision of 1500 ppm at 1.9 minutes cadence; I_c-filter observations). Data reduction for the OAA and OMC observations was performed in a two-step process: the `MaximDL` image processing software was used to perform image calibration (bias, darks, flats), while differential photometry was obtained using the `AstroImageJ` software (Collins et al. 2017). For the RCO observations, image calibration and differential photometry were both performed using `AstroImageJ`. The data, along with a best-fit model transit after subtracting the best-fit systematics model for each data set (see Section 3 for details), are presented in Figure 4. The data are also presented in Table 6.

The observed transits by these three independent observatories on 2020 May 21 not only confirmed that the event observed by TESS was on target (i.e., it happened on TOI-1759), but in practice confirmed that the real period of the event was 18.85 days (i.e., half the period proposed by the TESS data validation reports), with the duration and depth detected by those observatories being consistent with the duration and depth observed in the TESS transit events.

Long-term photometric monitoring was also performed from the ground using the 0.8 m Joan Oró telescope (TJO; Colomé et al. 2010) at the Montsec Observatory in Lleida, Spain and the 90 cm telescope at the Sierra Nevada Observatory (SNO; Amado et al. 2021). For the TJO observations, the data were obtained from 2020 June to 2021 April, spanning more than 300 days and covering 107 different nights. We obtained a total of 1331 images with an exposure time of 40 s using the Johnson R filter of the LAIA imager, a 4k × 4k CCD with a field of view of 30′ and a scale of 0.″4 pixel^{-1}. The SNO data were obtained from 2021 April to August, spanning 135 days and collecting observations on 55 different nights. Each night, 20 exposures per filter were obtained using both Johnson V and R filters, with exposure times of 60 and 40 s, respectively. The photometry from these exposures was averaged to obtain a single photometric value per filter each night. These data were obtained with a VersArray 2k × 2k CCD camera with a field of view of 13.2 × 13.2 arcmin^2 and a scale of 0.″4 pixel^{-1} as well.

The TJO CCD images were calibrated with darks, and bias and flat fields with the ICAT pipeline (Colome & Ribas 2006). The differential photometry was extracted with `AstroImageJ` (Collins et al. 2017) using the aperture size that minimized the rms of the resulting relative fluxes and a selection of the 30 brightest comparison stars in the field that did not show variability. Then, we used our own pipelines to remove outliers and measurements affected by poor observing conditions or presenting a low signal-to-noise ratio. This resulted in a total of 1087 measurements in the final data set with an rms of 6 parts per thousand (ppt).

In a similar way, the SNO resulting light curves were obtained by the method of synthetic aperture photometry. Each CCD frame was also corrected in a standard way for bias and flat-fielding. Different aperture sizes were tested in order to choose the best one for our observations. A number of nearby

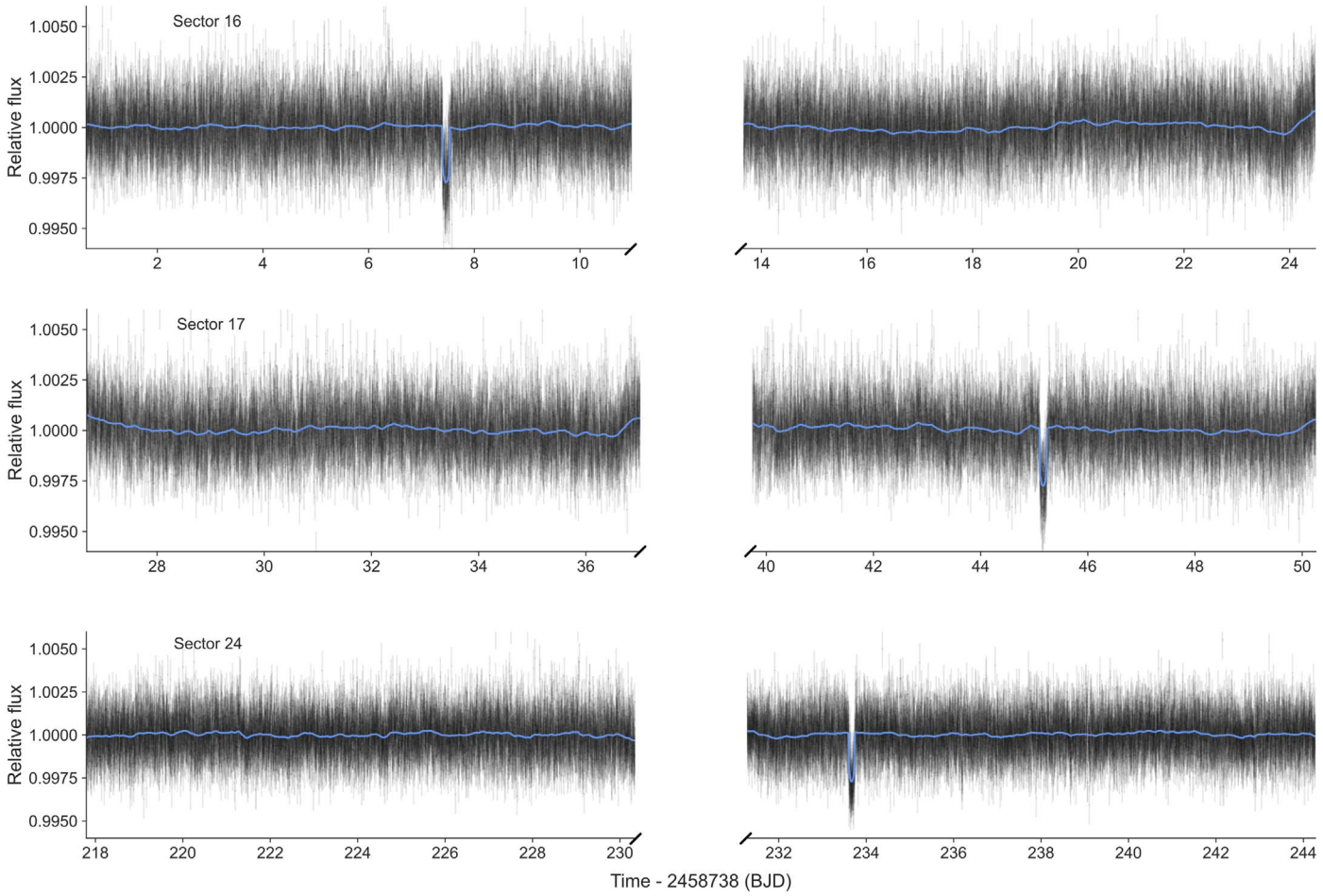

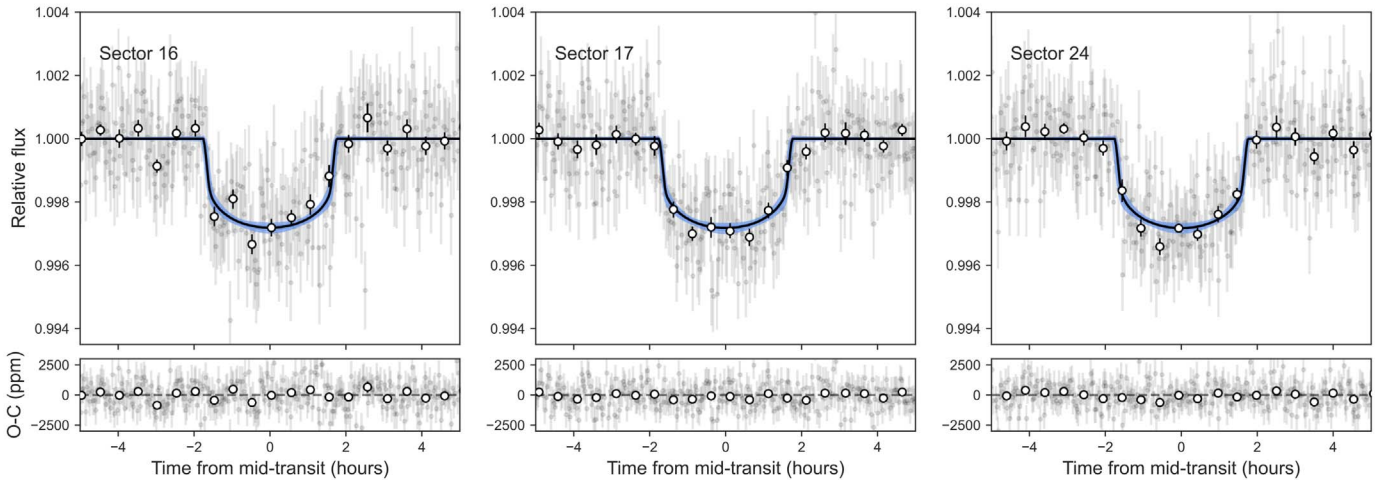

Figure 2. TESS transits of TOI-1759 b. The top panels present the TESS photometry of TOI-1759 in Sectors 16, 17, and 24 as a function of time (black points with error bars), along with the best-fit model, which consists of a transit model plus a Gaussian process (blue curve). Note there is only a single transit observed in each sector. The bottom panels shows a close-up to each of those transits, which have been phased around the time of midtransit (gray points with error bars); the Gaussian process component has been removed from this photometry. The black line in these panels show the best-fit transit model; blue bands represent the 68% and 95% credibility bands of the model.

and relatively bright stars within the frames were selected as reference stars to produce differential photometry of TOI-1759. Finally, outliers due to poor observing conditions or very high airmass were removed. This resulted in a total of 1029 and 1027 individual data points in filters V and R, respectively, with rms values of 6.1 and 6.4 ppt.

Both the TJO and SNO data sets are presented in Table 7. An analysis of these data sets is presented in Section 3.2.

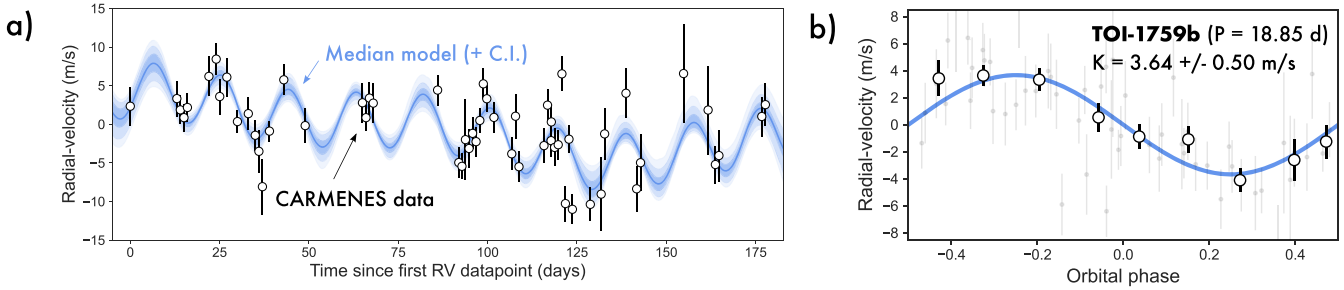

Figure 3. CARMENES radial-velocity follow-up of TOI-1759. (a) Our CARMENES radial-velocity campaign (white points with black error bars; first point corresponding to 2,459,054.56851) had a total duration of about 6 months, over which we were able to detect both a radial-velocity variation at 18.85 days, along with a long-term signal here modeled as a GP. The blue line with transparent bands around it indicate our full (GP + planetary) median signal, along with its 68%, 95%, and 99% credibility intervals, respectively. (b) Phase-folded radial-velocity curve at the period of the transiting exoplanet TOI-1759 b ($P = 18.85$ days; gray points, binned data points covering about 2 days plotted as white points with black error bars). The semiamplitude we obtain for this signal is 3.64 ± 0.50 m s^{-1}.

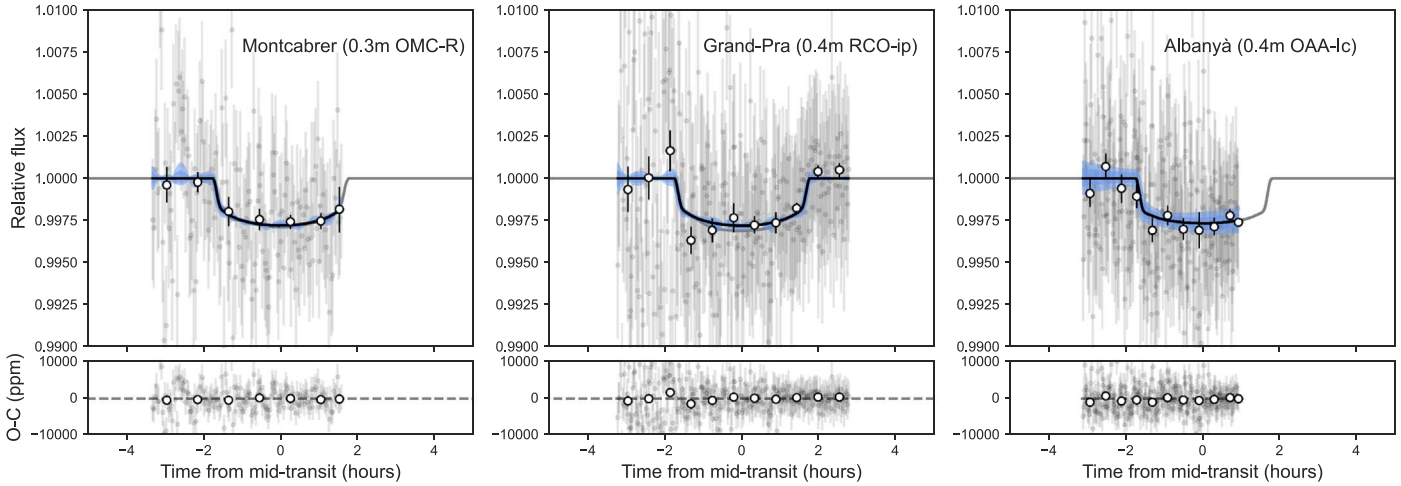

Figure 4. Ground-based follow-up transit photometry of TOI-1759 b. Transit of TOI-1759 b on 2020 May 21 captured by three different observatories: the OAA telescope of the Observatori Astronòmic Albanyà, the RCO telescope of the Grand-Pra Observatory, and the OMC telescope of the Montcabrer Observatori. The duration and depth of the event are consistent between instruments.

2.4. High-resolution Imaging

To help rule out stellar multiplicity and close blends with nearby stars and to obtain more precise planetary radii by accounting for close-in stellar blends (Ciardi et al. 2015; Schlieder et al. 2021), we observed TOI-1759 with both the 'Alopeke[39] speckle imaging camera (Scott & Howell 2018) on the 8 m Gemini North telescope and the NIRC2 near-infrared (NIR) adaptive-optics fed camera on the 10 m Keck II telescope. The optical and NIR high-resolution imaging complement each other with higher resolution in the optical but deeper sensitivity (especially to low-mass stars) in the infrared.

'Alopeke obtains diffraction-limited imaging in two simultaneously imaged narrow bands centered at 562 and 832 nm. Due to the relative faintness of the target star at these wavelengths, we obtained five exposures in each channel, with integration times of 60 ms each. We reduced the data using standard techniques using the methods described by Matson et al. (2019). The resulting contrast curves and reconstructed 832 nm image are all shown in Figure 5. The optical speckle observations show no evidence of an additional stellar companion.

TOI-1759 was observed with the NIRC2 instrument on Keck II behind the natural guide star AO system (Wizinowich et al. 2000). The observations were made on 2020 September 09 UT in the standard three-point dither pattern that is used with NIRC2 to avoid the left lower quadrant of the detector, which is typically noisier than the other three quadrants. The dither pattern step size was 3″ and was repeated twice, with each dither offset from the previous dither by 0.″5. The camera was in the narrow-angle mode with a full field of view of ∼10″ and a pixel scale of approximately 0.″0099 pixel^{-1}. The observations were made in the narrowband Brγ filter ($\lambda_o = 2.1686$; $\Delta\lambda = 0.0326$ μm) with an integration time of 1 s with one coadd per frame for a total of 9 s on target.

The AO data were processed and analyzed with a custom set of IDL tools. The science frames were flat-fielded and sky-subtracted. The flat fields were generated from a median average of dark-subtracted flats taken on-sky, and the flats were normalized such that the median value of the flats is unity. Sky frames were generated from the median average of the nine dithered science frames; each science image was then sky-subtracted and flat-fielded. The reduced science frames were combined into a single combined image using a intrapixel interpolation that conserves flux, shifts the individual dithered frames by the appropriate fractional pixels, and median coadds the frames. The final resolution of the combined dithers was determined from the FWHM of the point-spread function, 0.″049. The sensitivities of the final combined AO image were determined by injecting simulated sources azimuthally around

[39] https://www.gemini.edu/instrumentation/alopeke-zorro

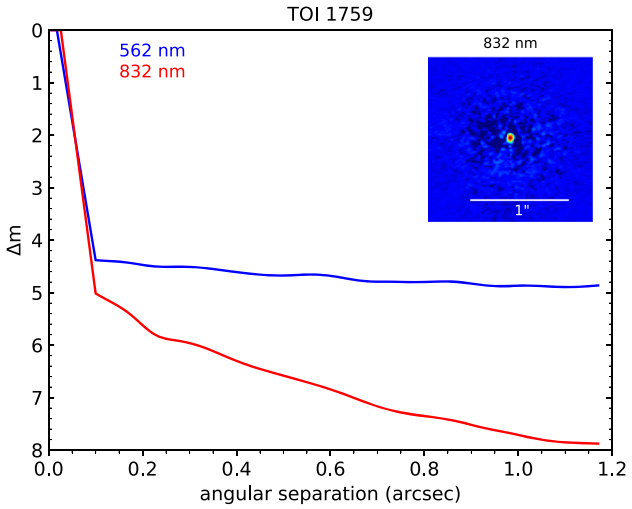

Figure 5. High spatial resolution imaging of TOI-1759. Two-band speckle imaging observations obtained with the 'Alopeke speckle imaging camera on the 8 m Gemini North telescope for TOI-1759 reveal no close companion down to 0.1″, dimmer than about $\Delta m = 4-5$ mag than the target.

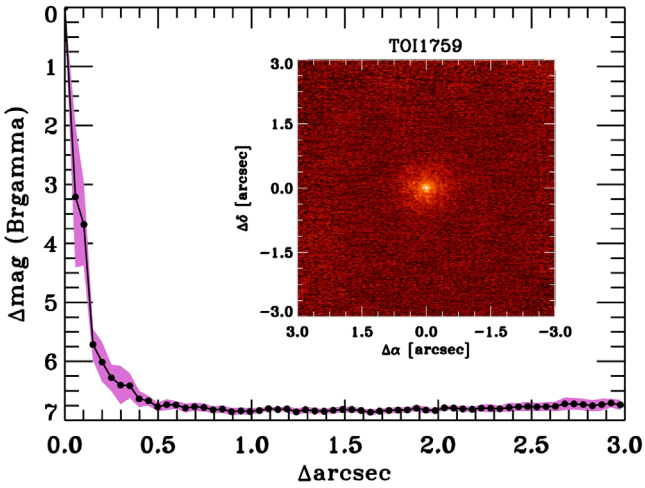

Figure 6. Near-infrared high spatial resolution imaging of TOI-1759. NIRC2 imaging observations obtained for TOI-1759 on Keck II reveals no close companion down to 0.1″, dimmer than about $\Delta m = 4-5$ mag than the target.

the primary target every 20° at separations of integer multiples of the central source's FWHM (Furlan et al. 2017). The brightness of each injected source was scaled until standard aperture photometry detected it with 5σ significance. The resulting brightness of the injected sources relative to the target set the contrast limits at that injection location. The final 5σ limit at each separation was determined from the average of all of the determined limits at that separation and the uncertainty on the limit was set by the rms dispersion of the azimuthal slices at a given radial distance. The final combined image and sensitivity curve are shown in Figure 6.

Both the optical speckle and the near-infrared adaptive-optics observations find no additional stars (down to 0.″1, dimmer by about 4–5 mag than the target in the optical and near-infrared) and so further strengthen the case for TOI-1759 b being a bona fide planet.

3. Analysis

3.1. Stellar Parameters

We obtained the photospheric parameters $T_{\rm eff}$, $\log g$, and [Fe/H] of TOI-1759 following Passegger et al. (2019) by fitting PHOENIX synthetic spectra to the combined (coadded) CARMENES VIS spectrum described in Section 2.2, which has a signal-to-noise ratio in the VIS channel of ≈200. We used $v \sin i = 2$ km s^{-1}, which was measured by Marfil et al. (2021) as an upper limit. We derived its luminosity following Cifuentes et al. (2020) by using the latest parallactic distance from Gaia EDR3 (Gaia Collaboration et al. 2021), and by integrating Gaia, 2MASS (Skrutskie et al. 2006), and AllWISE (Cutri et al. 2014) photometry covering the full spectral energy distribution with the Virtual Observatory Spectral energy distribution Analyzer (Bayo et al. 2008). The stellar radius follows from the Stefan−Boltzmann law and the stellar mass was determined using the linear mass–radius relation from Schweitzer et al. (2019).

TOI-1759's pseudo equivalent width of the Hα line as defined by Schöfer et al. (2019) is pEW′(Hα) < -0.3 Å (Marfil et al. 2021), classifying it as an Hα inactive star. Furthermore, Marfil et al. (2021) assign it to the Galactic thin disk population, which has a maximum age of about 8 Gyr (Fuhrmann 1998). Using these two properties as age indicators, we conclude that its age is between 1 Gyr (the typical minimum age for field stars) and 8 Gyr without being able to be more precise. All collected and derived parameters are presented in Table 1.

3.2. Radial-velocity Analysis

We performed a detailed analysis of the radial velocities described in Section 2.2 in order to constrain the possible signals arising from these data. To this end, we performed a suite of model fits to the radial-velocity data using `juliet` (Espinoza et al. 2019), in order to measure the evidence for a planet in the data using Bayesian evidences, $Z = P$ (Model | Data). The fits were performed using the Dynamic Nested Sampling algorithm implemented in the `dynesty` library (Speagle 2020).

We considered three main types of radial-velocity models. The first was a "no planet" model, namely, a set of models in which it is assumed there is no planetary signal present in the radial-velocity data, and which thus assumes the data are either consistent with a flat line or with correlated noise modeled through a Gaussian process (GP). The second class were "1 planet" models; these considered the presence of a planetary signal in the radial-velocity data (modeled as a circular orbit), and a suite of possible extra signals, such as linear or quadratic trends, or a (quasi-periodic) GP. Finally, we also considered the possibility that the data were best explained by a "2 planet" model, as a sum of two circular orbits and a suite of possible extra signals, such as a linear, quadratic, or GP trend.

We first performed "blind" fits to the data—that is, fits in which we assumed no strong prior knowledge on the signal(s) present on our radial velocities. For our GP, we assumed a quasi-periodic kernel of the form

$$k(t_i, t_j) = \sigma_{GP}^2 \exp\left(-\alpha\tau^2 - \Gamma \sin^2\left[\frac{\pi\tau}{P_{\rm rot}}\right]\right),$$

where $\tau = |t_i - t_j|$. We set log-uniform priors for σ_{GP}, α, and Γ, with lower and upper limits of (0.01, 100) m s^{-1}, (10^{-10}, 1) day^{-1} and (0.01, 100) respectively, based on the

Table 1
Stellar Properties of TOI-1759

Parameter	Value	Reference
Names	TIC 408636441	TIC
	2MASS J1472477+6245139	2MASS
	TYC 4266-00736-1	Tycho-2
	WISEA J214724.51+624513.8	AllWISE
R.A. (J2000)	$21^{h}47^{m}24\overset{s}{.}39$	Gaia EDR3
Decl. (J2000)	$62°45'13\overset{''}{.}7$	Gaia EDR3
Spectral type	M0.0 V	Lep13
$\mu_\alpha \cos\delta$ (mas yr^{-1})	-173.425 ± 0.012	Gaia EDR3
μ_δ (mas yr^{-1})	-10.654 ± 0.011	Gaia EDR3
π (mas)	24.922 ± 0.010	Gaia EDR3
d (pc)	40.112 ± 0.016	Gaia EDR3
G_{BP} (mag)	11.7164 ± 0.0029	Gaia EDR3
G (mag)	10.8386 ± 0.0028	Gaia EDR3
T (mag)	9.9284 ± 0.0073	TIC
G_{RP} (mag)	9.9174 ± 0.0038	Gaia EDR3
J (mag)	8.771 ± 0.043	2MASS
H (mag)	8.114 ± 0.059	2MASS
K_s (mag)	7.930 ± 0.020	2MASS
$W1$ (mag)	7.825 ± 0.027	AllWISE
$W2$ (mag)	7.886 ± 0.020	AllWISE
$W3$ (mag)	7.787 ± 0.018	AllWISE
$W4$ (mag)	7.643 ± 0.111	AllWISE
$L_\star$ ($10^{-4}\ L_\odot$)	876.7 ± 6.3	This work
$T_{\rm eff}$ (K)	4065 ± 51	This work
$\log g$ (dex)	4.65 ± 0.04	This work
[Fe/H] (dex)	0.05 ± 0.16	This work
$v \sin i$ (km s^{-1})	$\leqslant 2$	Mar21
$M_\star$ ($M_\odot$)	0.606 ± 0.020	This work
$R_\star$ ($R_\odot$)	0.597 ± 0.015	This work
Age (Gyr)	1–8	This work
$\rho_\star$ (kg m^{-3})	3949 ± 323	This work

References—2MASS (Skrutskie et al. 2006), AllWISE (Cutri et al. 2014), Gaia EDR3 (Gaia Collaboration et al. 2021), Lep13 (Lépine et al. 2013), Mar21 (Marfil et al. 2021), TIC (Stassun et al. 2019), Tycho-2 (Høg et al. 2000).

experiments performed with this kernel in Stock et al. (2020a) and Stock et al. (2020b), and a uniform prior for $P_{\rm rot}$ between 0.5 (half the best sampling in our radial velocities) and 350 days (two times our time baseline). The linear and quadratic trends both had uniform priors on the coefficients of $(10^{-3}, 10^{3})$. As for the circular orbits, we set a uniform prior on the period of the first one from 0.5 to 50 days (so as to cover the 18 and 36 days periods that could possibly originate from the transiting exoplanet), and a uniform prior on the period of the second one from 50 to 350 days. Uniform priors were set for the time of inferior conjunction to cover the entire time baseline of our observations, the semiamplitude—between 0 and 100 m s^{-1}—and the systematic radial velocity—between -100 and 100 m s^{-1}. A jitter term, σ_w was added to all of our fits with a log-uniform prior between 0.01 and 100 m s^{-1}.

In our "blind" fits, we found that all models considering a periodic component were consistent with a prominent signal at ∼18.5 days, which corresponds to the transit signal implied by the TESS photometry presented in Section 2.1 and the ground-based transits presented in Section 2.3. The model with the highest evidence in our set of fits was one composed of a sinusoid plus a quasi-periodic GP ($|\Delta \log Z| \approx 4.3$, compared with the no-planet model). Given the high-resolution imaging data presented in Section 2.4, the ground-based transit detected on target presented in Section 2.3, and the fact that the period of the planetary signal for the model with the highest evidence ($18.49^{+0.23}_{-0.21}$ days) agrees with the period implied by the photometric data (18.8480 ± 0.0010 days), we consider that this 18 days period signal in both photometry and radial velocities is, indeed, a bona fide transiting exoplanet.

Table 2
Log-evidence Differences ΔZ between Different Models Considered for Our Radial-velocity-only Analysis

Model	$\ln \Delta Z$
No planet models	
Flat line	−9.4
GP	−6.6
1 planet models	
1 planet + linear trend	−23.6
1 planet + quadratic trend	−9.1
1 planet	−8.8
1 planet + GP	0
2 planet models	
2 planet + linear trend	−12.6
2 planet	−1.6
2 planet + GP	−1.4
2 planet + quadratic trend	−1.3

Note. It is assumed that one of the Keplerian signals has the same ephemerides as those implied by the observed transits. A flat-line model includes only a systematic radial velocity and a jitter term. The GP refers to a Gaussian Process with a quasi-periodic kernel. See text for details on the priors.

Having concluded that the 18 days period signal is indeed a bona fide transiting exoplanet, we then focused on finding the best model that explains the radial-velocity data set. We considered the same class of models and priors as the ones presented above, but now for the first planet we fixed the period and transit center to the values defined by a photometric fit made to the data using `juliet` (see Section 3.3 for details on the priors of that fit): period $P = 18.85008 \pm 0.00018$ days, and time-of-transit center $t_0 = 2{,}458{,}745.4651 \pm 0.0015$ days. A compilation of the log-evidences for each of the fits we performed is presented in Table 2. As can be seen, the model with the highest evidence is once again a 1 planet + GP model. Interestingly, however, this model is in practice indistinguishable ($|\Delta \log Z| < 2$; Trotta 2008) from most of the 2 planet models (except the 2 planet + linear trend model). It is also indistinguishable from all of those models considering either one or both of them having eccentric orbits.

It is interesting to note that the posterior distribution function of the GP rotation period of the 1 planet + GP model, $P_{\rm rot}$, shows a bimodal distribution, with peaks at ∼80 days and >150 days. In the 2 planet + GP model, the latter long periodic signal is picked up by the second sinusoid and is constrained to be about 270 ± 60 days, while the quasi-periodic component of the GP shows again an accumulation of samples with a higher likelihood at ∼80 days. A Generalized Lomb−Scargle (GLS; Zechmeister & Kürster 2009) periodogram analysis of the residuals of each of those models is presented in Figure 7, in order to further explore the nature of these long-period signals. If the signal of the transiting planet is subtracted (second panel), a significant power excess is apparent at ∼270 days (which is above the baseline of our observations, which was

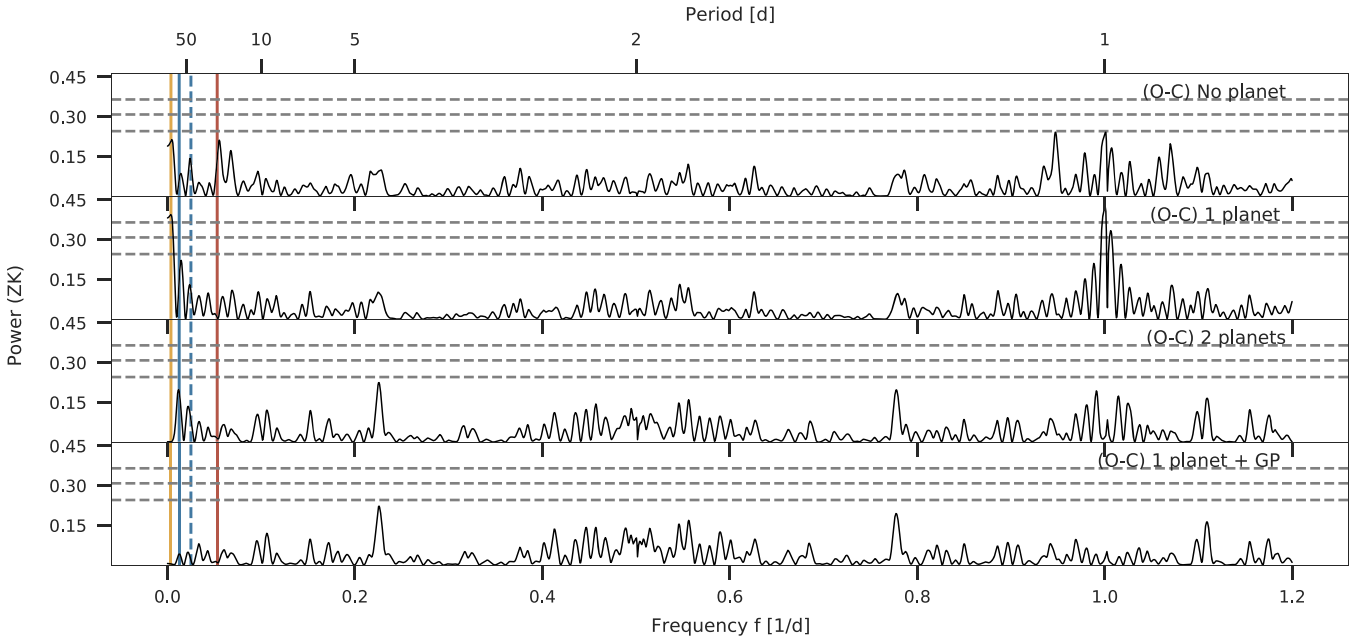

Figure 7. Generalized Lomb−Scargle (GLS) periodograms of the CARMENES radial-velocity data after subtracting different models. The power at each frequency corresponds to the one defined in Zechmeister & Kürster (2009; ZK in the labels above). The period of the transiting planet, $P = 18.85$ days, is marked by the red solid line and the stellar rotation period, $P \approx 80$ days, and its first harmonic are shown with the blue solid and dashed lines, respectively. Further, the additional present long-term periodicity with $P \approx 270$ days is marked by the yellow solid line. The horizontal dashed gray lines show the analytical false-alarm probabilities (FAP) of 10%, 1%, and 0.1%. The top panel corresponds to the mean-subtracted CARMENES radial-velocity data set.

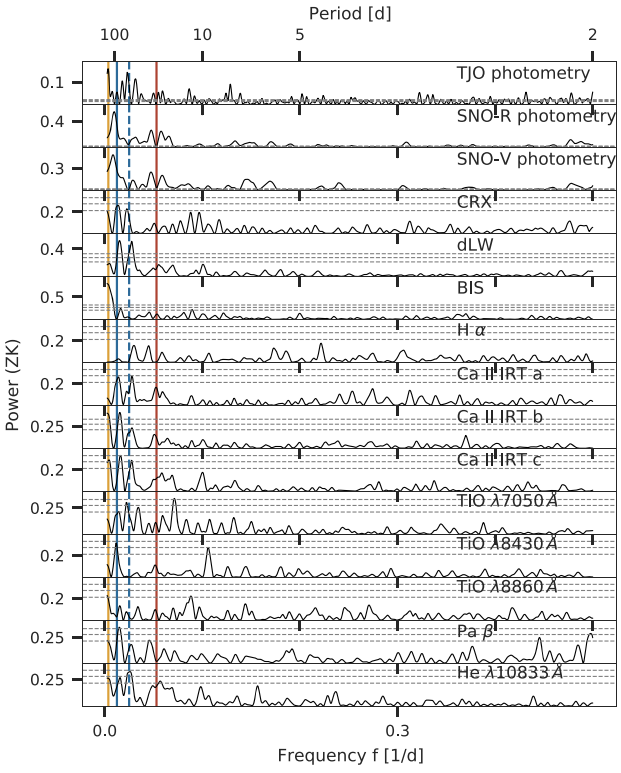

Figure 8. GLS periodograms of the TJO photometry, SNO photometry, and the CARMENES spectral activity indicators. Analogous to the periodograms of the RVs, the period of the transiting planet, $P = 18.85$ days, and the additional present long-term periodicity with $P \approx 270$ days are marked by the solid red and yellow lines, respectively. The stellar rotation period, $P \approx 80$ days, and its first harmonic are indicated by the blue solid and dashed lines. The horizontal dashed gray lines show the analytical false-alarm probabilities (FAP) of 10%, 1%, and 0.1%.

175 days), and next to it, even though it is insignificant, is a peak at ∼80 days. The latter is independent of the long-term variation, as it is still present after fitting the transiting planet together with the ∼270 days signal (third panel).

To find out whether the ∼80 days signal or the ∼270 days power excess could be attributed to stellar activity, we investigated the activity indicators that are routinely derived from the CARMENES spectra (see Zechmeister et al. 2018; Schöfer et al. 2019; Lafarga et al. 2020, for the full list of indicators and how they are calculated). In Figure 8 we show the GLS periodograms of several activity indicators and the long-term photometry presented in Section 2.3. Almost all indicators, as well as the photometry, show consistent signals around 80 and/or 40 days, which would explain the ∼80 days seen in the radial velocities (RVs) as the stellar rotation period. If indeed the rotation period of the star is 80 days, the 40 days signal could be interpreted as spots at opposite longitudes and/or a byproduct of the not strictly periodic nature of the signal. Further, the TJO data, the BIS, and the Ca II IRT b and c also show a long-term trend, which might be related with the ∼270 days power excess.

Given that we could not rule out a stellar origin for the ∼80 days signal and the ∼270 days power excess, and that the 1 planet + GP model has the highest evidence for our RV data and can account for all significant signals in the data (see the residuals in the last panel of Figure 7), we consider this model for the global modeling of the data, which we present in the next subsection. We note that we also tested fitting our global model using the rest of the models in Table 2, which are indistinguishable from the one selected here, and all of them gave rise to similar constraints to the final parameters of the transiting exoplanet.

3.3. Global Modeling

We performed a global modeling of the radial-velocity and photometric data using the `juliet` library (Espinoza et al. 2019) in order to jointly constrain the planetary properties from the photometry and radial-velocity data sets outlined in previous sections. As in the radial-velocity analysis presented in Section 3.2, we once again used the Dynamic Nested Sampling algorithm implemented in the `dynesty` library (Speagle 2020).

For the TESS photometry, we decided to use a GP to consider residual systematic trends in the PDC light curves used in this work. We used an Exponential−Matérn kernel (i.e., the product of an exponential and a Matérn 3/2 kernel) as implemented in the `celerite` library (Foreman-Mackey et al. 2017) via `juliet`, with hyperparameters (GP amplitude, σ_{GP}, and two timescales,: one for the Matèrn 3/2 part of the kernel, ρ, and another for the exponential part of the kernel, T), which are individual to each of the sectors; a jitter term was also added in quadrature to the covariance matrix for each sector. A quadratic law was used to constrain limb darkening, where the coefficients were shared between the different sectors; we used the parameterization of Kipping (2013) instead of fitting for the limb-darkening coefficients directly. For the ground-based photometry, we found that airmass was a very good predictor of the long-term trends in the data, and so we added this as a linear regressor in our fit—weighted by a coefficient θ, which was different for each instrument and was jointly fit with the rest of the parameters of the global fit. In addition, we observed that this linear regressor was insufficient to model all of the correlated noise leftover on the OMC and RCO data sets. We thus decided to fit those with an additional Matèrn 3/2 kernel. A linear limb-darkening law was used for all ground-based instruments, as a higher-order law was not necessary given the lower photometric precision (see, e.g., Espinoza & Jordán 2016). An individual jitter term was added to the diagonal of the covariance matrix on each of those data sets as well. For the radial velocities, following our results in Section 3.2, we considered a 1 planet model plus a quasi-periodic GP as the model to be fit in our joint analysis. We set a wide prior for the systemic radial velocity, as well as for the jitter term and the hyperparameters of the GP—in particular, for the period of the quasi-periodic GP $P_{\rm rot}$, we use a wide period of between 20 and 350 days in order to cover the two possible periods for this parameter observed in Section 3.2. The full definition of the priors and corresponding posteriors of our joint fit are given in Table 3.

The resulting best-fit models and corresponding credibility bands are presented in Figure 2 for the TESS photometry, in Figure 4 for the ground-based photometry, and in Figure 3 for the radial velocities. The constraints from our radial-velocity follow-up allowed us to obtain a precise ($>5\sigma$ above 0) measurement of the semiamplitude imprinted by TOI-1759 b on its star of $K = 3.64^{+0.50}_{-0.51}$ m s^{-1}, which is an over 7σ detection of the semiamplitude. Joining the derived transit and radial-velocity parameters, along with the stellar properties presented in Table 1, we derive the fundamental parameters of TOI-1759 b in Table 4. As can be observed, TOI-1759 b is a relatively cool (443 K equilibrium temperature, assuming 0 albedo) sub-Neptune-sized exoplanet ($R_p = 3.14 \pm 0.10\,R_\oplus$). Coupling these numbers with our estimated mass of $M_p = 10.8 \pm 1.5 M_\oplus$, we derive a planetary bulk density ($\rho_p = 1.91 \pm 0.32$ g cm^{-3}) and gravity ($g_p = 10.7 \pm 1.6$ m s^{-2}) that are strikingly similar to those of Neptune (1.64 g cm^{-3} and 11.15 m s^{-2}, respectively). We discuss the properties of TOI-1759 b in the context of other discovered systems in the next section.

Table 3
Prior and Posterior Parameters of the Global Fit Performed on TOI-1759

Parameter	Prior	Posterior
Stellar and planetary parameters		
P_1 (days)	$N(18.85, 0.1^2)$	18.85019 ± 0.00013
$t_{0,1}$ (BJD)	$N(2{,}458{,}745.45, 0.1^2)$	$2{,}458{,}745.4654 \pm 0.0011$
$R_{p,1}/R_\star$	$U(0.0, 1.0)$	0.0483 ± 0.0010
$b_1 = (a/R_\star)\cos(i)$	$U(0.0, 1.0)$	$0.21^{+0.09}_{-0.10}$
K_1 (m s^{-1})	$U(0, 100)$	$3.64^{+0.50}_{-0.51}$
e_1	fixed	0
ω_1	fixed	90
$\rho_\star$ (kg m^{-3})	$TN(3949, 323^2; 1000, 10{,}000)$	3970^{+218}_{-233}
TESS photometry instrumental parameters		
$q_{1,\rm TESS}$[a]	$U(0, 1)$	$0.32^{+0.24}_{-0.14}$
$q_{2,\rm TESS}$[a]	$U(0, 1)$	$0.46^{+0.28}_{-0.25}$
$m_{\rm flux,16}$ (ppm)	$U(0, 10^5)$	851^{+7916}_{-7770}
$m_{\rm flux,17}$ (ppm)	$U(0, 10^5)$	-1598^{+8062}_{-8089}
$m_{\rm flux,24}$ (ppm)	$U(0, 10^5)$	428^{+7904}_{-7797}
$\sigma_{\rm w,16}$ (ppm)	$\log U(0.1, 10^5)$	$1.8^{+7.5}_{1.5}$
$\sigma_{\rm w,17}$ (ppm)	$\log U(0.1, 10^5)$	$2.9^{+15.1}_{-2.5}$
$\sigma_{\rm w,24}$ (ppm)	$\log U(0.1, 10^5)$	$1.9^{+7.7}_{1.6}$
$\sigma_{\rm GP,16}$ (ppm)	$\log U(10^{-4}, 10^2)$	$0.000104^{+0.000047}_{-0.0000026}$
$\sigma_{\rm GP,17}$ (ppm)	$\log U(10^{-4}, 10^2)$	$0.000106^{+0.000067}_{-0.0000040}$
$\sigma_{\rm GP,24}$ (ppm)	$\log U(10^{-4}, 10^2)$	$0.000100^{+0.000030}_{-0.0000017}$
$\rho_{\rm GP,16}$ (days)	$\log U(10^{-3}, 10^2)$	73^{+16}_{-17}
$\rho_{\rm GP,17}$ (days)	$\log U(10^{-3}, 10^2)$	74^{+15}_{-18}
$\rho_{\rm GP,24}$ (days)	$\log U(10^{-3}, 10^2)$	76^{+14}_{-17}
$T_{\rm GP,16}$ (days)	$\log U(10^{-3}, 10^2)$	$0.0010^{+0.000047}_{-0.000026}$
$T_{\rm GP,17}$ (days)	$\log U(10^{-3}, 10^2)$	$0.0011^{+0.000081}_{-0.000045}$
$T_{\rm GP,24}$ (days)	$\log U(10^{-3}, 10^2)$	$0.0010^{+0.000034}_{-0.000019}$
Ground-based photometry instrumental parameters		
$q_{1,\rm OAA}$	$U(0, 1)$	$0.41^{+0.27}_{-0.24}$
$q_{1,\rm OMC}$	$U(0, 1)$	$0.55^{+0.27}_{-0.31}$
$q_{1,\rm RCO}$	$U(0, 1)$	$0.50^{+0.30}_{-0.29}$
$m_{\rm flux,OAA}$ (ppm)	$U(0, 10^5)$	-2148^{+214}_{-216}
$m_{\rm flux,OMC}$ (ppm)	$U(0, 10^5)$	7936^{+6471}_{-6203}
$m_{\rm flux,RCO}$ (ppm)	$U(0, 10^5)$	-979^{+6296}_{-5945}
$\sigma_{\rm w,OAA}$ (ppm)	$\log U(0.1, 10^5)$	3395^{+146}_{-140}
$\sigma_{\rm w,OMC}$ (ppm)	$\log U(0.1, 10^5)$	3123^{+202}_{-190}
$\sigma_{\rm w,RCO}$ (ppm)	$\log U(0.1, 10^5)$	4143^{+165}_{-158}
$\theta_{\rm OAA}$ (days)	$U(-10, 10)$	$0.00112^{+0.00022}_{-0.00021}$
$\theta_{\rm OMC}$ (days)	$U(-10, 10)$	$-0.0036^{+0.015}_{-0.015}$
$\theta_{\rm RCO}$ (days)	$U(-10, 10)$	$0.013^{+0.015}_{-0.015}$
$\sigma_{\rm GP,OMC}$ (ppm)	$\log U(10^{-4}, 10^2)$	$0.117^{0.022}_{-0.012}$
$\rho_{\rm GP,OMC}$ (days)	$\log U(10^{-3}, 10^2)$	$0.438^{+0.040}_{-0.059}$
$\sigma_{\rm GP,RCO}$ (ppm)	$\log U(10^{-4}, 10^2)$	$0.117^{0.019}_{-0.011}$
$\rho_{\rm GP,RCO}$ (days)	$\log U(10^{-3}, 10^2)$	$0.438^{+0.039}_{-0.051}$
Radial-velocity instrumental/activity parameters		
$\mu_{\rm CARMENES}$ (m s^{-1})	$U(-100, 100)$	$0.1^{+4.7}_{4.0}$
$\sigma_{w,\rm CARMENES}$ (m s^{-1})	$\log U(0.01, 100)$	$1.85^{+0.50}_{-0.49}$
$\sigma_{\rm GP,CARMENES}$ (m s^{-1})	$\log U(0.01, 10^2)$	$5.8^{+7.3}_{-2.5}$
$\alpha_{\rm GP,CARMENES}$ (days^{-1})	$\log U(10^{-10}, 1)$	$0.000011^{+0.000433}_{-0.000011}$
$\Gamma_{\rm GP,CARMENES}$	$\log U(0.01, 100)$	$0.5^{+2.8}_{-0.5}$
$P_{\rm GP,Rot}$	$U(20, 350)$	237^{+67}_{-103}

Note. For the priors, $N(\mu, \sigma^2)$ stands for a normal distribution with mean μ and variance σ^2; $TN(\mu, \sigma^2; a, b)$ is a truncated normal distribution with lower and upper limits given by a and b, respectively; $U(a, b)$ and $\log U(a, b)$ stand for a uniform and log-uniform distribution between a and b, respectively.
[a] These parameterize the quadratic limb-darkening law using the transformations in Kipping (2013).

Table 4
Derived Properties for TOI-1759 b

Parameter	Posterior	Description
R_p ($R_\oplus$)	3.14 ± 0.10	Planetary radius
M_p ($M_\oplus$)	10.8 ± 1.5	Planetary mass
i (degrees)	89.72 ± 0.13	Orbital inclination
T_{14} (hrs)	3.23 ± 0.13	Transit duration
a (au)	0.1177 ± 0.0038	Semimajor axis of the orbit
$T_{\rm eq,0}$ (K)	443 ± 7	Equilibrium temperature[a] (assuming 0 albedo)
$T_{\rm eq,0.3}$ (K)	405 ± 6	Equilibrium temperature[a] (assuming 0.3 albedo)
S_p ($S_\oplus$)	6.39 ± 0.41	Stellar irradiation on the plane
ρ_p (g cm^{-3})	1.91 ± 0.32	Planetary bulk density
g_p (m s^{-2})	10.7 ± 1.6	Planetary surface gravity

Note.
[a] This assumes a perfect energy redistribution.

4. Discussion

In order to put TOI-1759 b in context with the known sample of small exoplanets, we query the properties of all such exoplanets that (a) have both a measured mass and radius, (b) are smaller than $R_p < 4\,R_\oplus$, and (c) have equilibrium temperatures cooler than 1000 K from the NASA Exoplanet Archive (NASA Exoplanet Science Institute 2020)—i.e., a cut similar to that presented in Guo et al. (2020), but updated with the latest exoplanetary systems as of 2021 July 23.[40] In Figure 9, we show the location of TOI-1759 b in both the planetary mass versus radius plane and the equilibrium temperature versus planetary radius plane.

In terms of the mass and radius, Figure 9(a) shows that TOI-1759 b is consistent with having a 2%–5% H_2 envelope and an interior composition ranging from being an Earth-like one to being a scaled-down version of Neptune. Figure 9(b), by contrast, shows how TOI-1759 b adds to the increasing number of small ($R_p < 4\,R_\oplus$) worlds with a measured mass and radius at relatively low equilibrium temperatures. In particular, TOI-1759 b falls in the very interesting region in which it has been proposed (Yu et al. 2021) that exoplanet atmospheres are hazy, due to the lack of haze-removal processes at temperatures of between about 300 and 600 K. It is interesting to note that TOI-1759 b falls *exactly* at the equilibrium temperature at which Yu et al. (2021) predict the haziest exoplanets should be ($T_{\rm eq,0.3} \sim 400$ K, where $T_{\rm eq,0.3}$ means an equilibrium temperature calculated assuming an albedo of 0.3; see Table 4). The proposed trend presented in that work seems to be in line with observed transmission spectra for planets hotter than about 500 K (Crossfield & Kreidberg 2017). For example, GJ 1214 b (550 K; Kreidberg et al. 2014; biggest red circle in Figure 9(a)) shows a significantly muted water feature, whereas HAT-P-11 b (750 K; Fraine et al. 2014; not shown in Figure 9(a) as $R_p = 4.3\,R_\oplus$ for this exoplanet) has a 3-scale-height water amplitude in its transmission spectrum. However, the hypothesis is harder to test for temperate exoplanets (<500 K), as good targets for atmospheric characterization have remained scarce, in particular for small ($R_p < 4\,R_\oplus$) planets.

[40] More recent queries, along with the same plots shown here, can be generated using the scripts in this repository: https://github.com/nespinoza/warm-worlds.

TOI-1759 b is among the best temperate targets to perform transmission spectroscopy based on its transmission spectroscopy metric (TSM; Kempton et al. 2018). Following the work of Kempton et al. (2018), we estimate a TSM of 81 ± 14, which puts it among the top five targets for atmospheric characterization to date at equilibrium temperatures lower than 500 K, together with L 98-59 d (TSM of 233; Cloutier et al. 2019; Kostov et al. 2019; Pidhorodetska et al. 2021), TOI-178 g (TSM of 114; Leleu et al. 2021), TOI-1231 b (TSM of 97; Burt et al. 2021), and LHS 1140 b (TSM of 89; Dittmann et al. 2017; Ment et al. 2019)—the latter actually having been recently characterized by HST/WFC3 data (Edwards et al. 2021), with weak evidence for water absorption in its planetary atmosphere.

For a quantitative assessment of TOI-1759 b's atmospheric characterization with the James Webb Space Telescope (JWST), we investigated a suite of atmospheric scenarios and calculated their JWST synthetic spectra using the photochemical model ChemKM (Molaverdikhani et al. 2019, 2020a), the radiative transfer model petitRADTRANS (Mollière et al. 2019, 2020), and `ExoTETHyS` (Morello et al. 2021) for uncertainty estimations.

Assuming an isothermal atmosphere with a temperature of 400 K and a constant vertical mixing of $K_{zz} = 10^6$ cm^2 s^{-1} results in persistent water and methane features in the transmission spectra of TOI-1759 b; see Figure 10. But such atmospheric features are expected to be suppressed in a high-metallicity atmosphere; see the bottom panel in Figure 10. Considering haze in the atmosphere of TOI-1759 b further mutes the features, and hence a hazy, high-metallicity atmosphere is expected to show a nearly flat transmission spectrum; see the blue line in Figure 10, bottom panel.

The `PandExo` package (Batalha et al. 2017) was used to determine the best configurations to observe with the NIRISS SOSS (0.6–2.8 μm), NIRSpec G395M (2.88–5.20 μm), and MIRI LRS (5–12 μm) instrumental modes. Then, we used `ExoTETHyS` to compute the simulated spectra. The wavelength bins were specifically determined to have similar counts, leading to nearly uniform error bars per spectral point. Note that the minimal error bars output by `ExoTETHyS` have been multiplied by the reciprocal of the square root of the observing efficiency and a conservative factor of 1.2 that accounts for correlated noise. The resulting error bars are equal to or slightly larger than those obtained with `PandExo` for the same wavelength bins. In particular, the spectral error bars estimated for just one transit observation per instrument configuration are 25–30 ppm at wavelengths <5 μm, and 45–50 ppm at wavelengths >5 μm, with several points to sample each molecular feature (as shown in Figure 10). Comparing these uncertainties with the expected water and methane features of ~200 ppm significance suggests the possibility of differentiating these scenarios during one transit only.

TOI-1759 b, along with TOI-178 g ($R_p = 2.87\,R_\oplus$, $T_{\rm eq,0} = 470$ K), TOI-1231 b ($R_p = 3.65\,R_\oplus$, $T_{\rm eq,0} = 330$ K), and the (now) iconic K2-18 b ($R_p = 2.61\,R_\oplus$, $T_{\rm eq,0} = 255$ K; Benneke et al. 2019; Tsiaras et al. 2019) form an excellent sample of sub-Neptunes to perform atmospheric characterization via transmission spectroscopy at equilibrium temperatures of below 500 K. A sample that can be used to put the prediction of both proposed haze-removal (Yu et al. 2021) and methane removal (Molaverdikhani et al. 2020b) processes to the test.

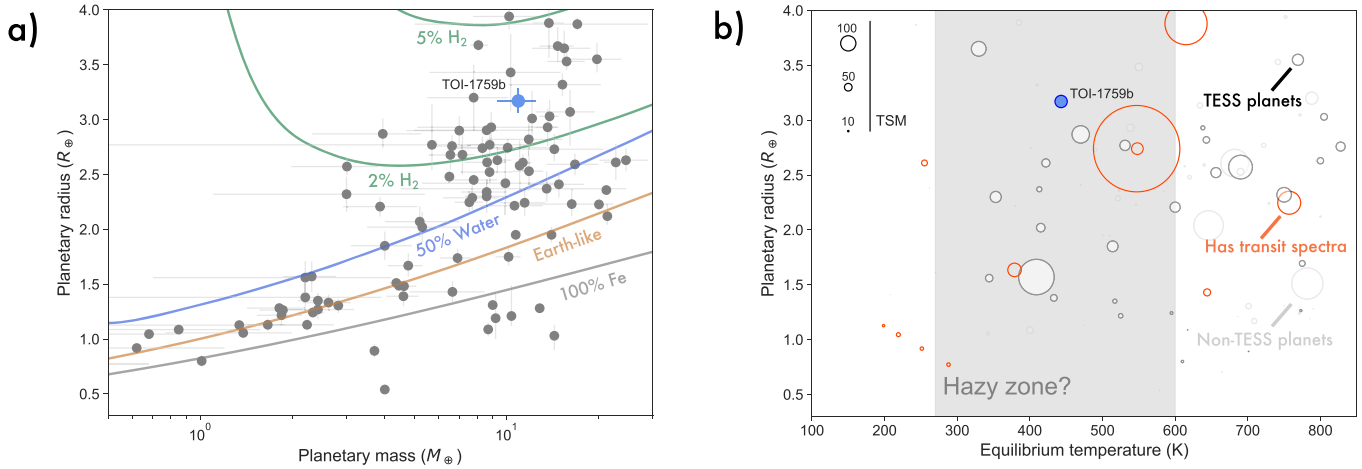

Figure 9. Properties of TOI-1759 b as compared to previously small, known exoplanets with a measured mass and radius. (a) Mass−radius diagram of all known small ($R_p < 4\,R_\oplus$) exoplanets with $T_{\rm eq} < 1000$ K (gray) and TOI-1759 b (blue). The mass–radius models are from Zeng et al. (2016) and show 100% Fe (gray), an Earth-like composition (32.5% Fe, 67.5% $MgSiO_3$ by mass; brown), a 50% Earth-like and 50% water-by-mass composition (blue), and Earth-like composition models with 2% and 5% H_2 on top of it (green). Water-rich models with 2% and 5% H_2 on top (i.e., Neptune-like compositions) are not shown, but would be indistinguishable from the green models in this panel given the size of the error bars. (b) Equilibrium temperature (assuming zero albedo) vs. radius diagram for the same cuts made for panel (a), showing the location of TESS planets (white markers), non-TESS planets (white transparent markers), planets that have previously been characterized via transmission spectroscopy with WFC3 on the Hubble Space Telescope (HST; red markers) and TOI-1759 b (blue). The size of the markers represents the value of the transmission spectroscopy metric (TSM; Kempton et al. 2018); the gray band shows the proposed region of hazy exoplanets by Yu et al. (2021; see text for discussion).

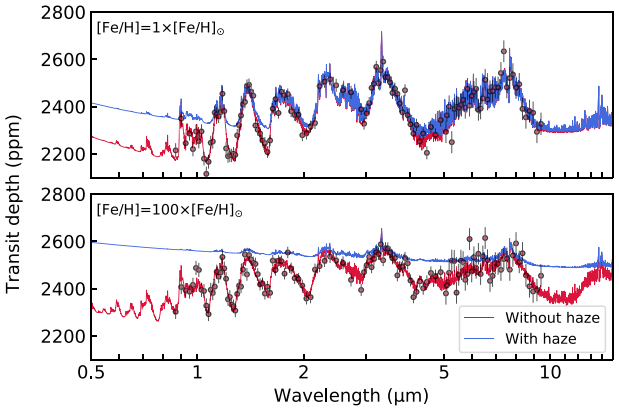

Figure 10. Synthetic JWST transmission atmospheric spectra of TOI-1759 b. Top: fiducial models with solar abundance. Bottom: enhanced metallicity by a factor of 100, considering haze opacity (solid blue lines) and no haze opacity (solid red lines). Estimated uncertainties are shown for the observation of one transit with JWST NIRISS-SOSS, NIRSpec-G395M, and MIRI-LRS configurations.

5. Conclusions

We have presented the discovery and characterization of the transiting exoplanet TOI-1759 b, a sub-Neptune ($R_p = 3.14 \pm 0.10\,R_\oplus$, $M_p = 10.8 \pm 1.5\,M_\oplus$) exoplanet on a 18.85 days orbit around an M-dwarf star. The initial identification of the target was made thanks to precise TESS photometry, which unveiled three transits of the exoplanet in three different sectors with an ambiguous period being consistent with both a 18.85 and a 37.7 days period exoplanet. Thanks to ground-based photometric follow-up from different observatories, high-resolution spatial imaging, and precise radial velocities from the CARMENES high-resolution spectrograph, we were able to not only confirm TOI-1759 b as a bona fide transiting exoplanet and precisely measure its mass, but also constrain its true period to be 18.85019 ± 0.00013 days.

TOI-1759 b adds to the growing number of temperate ($T_{\rm eq} < 500$ K) exoplanets and is a particularly promising target on which to perform atmospheric characterization. Its equilibrium temperature ($T_{\rm eq,0.3} = 405 \pm 6$ K) puts it exactly where the work of Yu et al. (2021) predicts the haziest exoplanets to be, and thus provides an exciting system in which to test this proposal. In addition, our 6 month radial-velocity campaign revealed an 80 days periodicity in the data most likely arising from stellar activity, and a possible longer-term periodicity with a period of >200 days. The current baseline of our CARMENES observations is insufficient to unveil the true nature of this latter long-period signal. However, a campaign spanning a longer baseline is needed in order to reveal the exact source and periodicity of this signal.

CARMENES is an instrument at the Centro Astronómico Hispano-Alemán (CAHA) at Calar Alto (Almería, Spain), operated jointly by the Junta de Andalucía and the Instituto de Astrofísica de Andalucía (CSIC). CARMENES was funded by the Max-Planck-Gesellschaft (MPG), the Consejo Superior de Investigaciones Científicas (CSIC), the Ministerio de Economía y Competitividad (MINECO), and the European Regional Development Fund (ERDF) through projects FICTS-2011-02, ICTS-2017-07-CAHA-4, and CAHA16-CE-3978, and the members of the CARMENES Consortium (Max-Planck-Institut für Astronomie, Instituto de Astrofísica de Andalucía, Landessternwarte Königstuhl, Institut de Ciëncies de l'Espai, Institut für Astrophysik Göttingen, Universidad Complutense de Madrid, Thüringer Landessternwarte Tautenburg, Instituto de Astrofísica de Canarias, Hamburger Sternwarte, Centro de Astrobiología, and Centro Astronómico Hispano-Alemán), with additional contributions by the MINECO, the Deutsche Forschungsgemeinschaft through the Major Research Instrumentation Programme and Research Unit FOR2544 "Blue Planets around Red Stars," the Klaus Tschira Stiftung, the states of Baden-Württemberg and Niedersachsen, and by the Junta de Andalucía. This work was based on data from the CARMENES data archive at CAB (CSIC-INTA). We acknowledge financial support from the Agencia Estatal de Investigación of the Ministerio de Ciencia, Innovación y Universidades and the ERDF through projects

PID2019-109522GB-C5[1:4], PGC2018-098153-B-C33, AYA2018-84089, PID2019-107061GB-C64, PID2019-110689RB-100, AYA2016-79425-C3-1/2/3-P, and BES-2017-080769, and the Centre of Excellence "Severo Ochoa" and "María de Maeztu" awards to the Instituto de Astrofísica de Canarias (CEX2019-000920-S), Instituto de Astrofísica de Andalucía (SEV-2017-0709), and Centro de Astrobiología (MDM-2017-0737), NASA (NNX17AG24G), and the Generalitat de Catalunya/CERCA program. Data were partly collected with the 90 cm telescope at the Sierra Nevada Observatory (SNO) operated by the Instituto de Astrofí fica de Andalucí a (IAA, CSIC). We acknowledge the telescope operators from the Sierra Nevada Observatory for their support. G.M. has received funding from the European Union's Horizon 2020 research and innovation program under the Marie Sklodowska-Curie grant agreement No 895525. This research has made use of the NASA Exoplanet Archive, which is operated by the California Institute of Technology, under contract with the National Aeronautics and Space Administration under the Exoplanet Exploration Program. We acknowledge the use of public TESS data from pipelines at the TESS Science Office and at the TESS Science Processing Operations Center. Resources supporting this work were provided by the NASA High-End Computing (HEC) Program through the NASA Advanced Supercomputing (NAS) Division at Ames Research Center for the production of the SPOC data products. The authors wish to recognize and acknowledge the very significant cultural role and reverence that the summit of Maunakea has always had within the indigenous Hawaiian community. We are most fortunate to have the opportunity to conduct observations from this mountain.

Facilities: TESS, CARMENES/3.5-m Calar Alto telescope, TJO, SNO, AAM, MONTSEC, Keck telescope, Gemini-North telescope.

Software: radvel (Fulton et al. 2018), batman (Kreidberg 2015), juliet (Espinoza et al. 2019), astroimagej (Collins et al. 2017), tpfplotter (Aller et al. 2020), dynesty (Speagle 2020), celerite (Foreman-Mackey et al. 2017).

Appendix A
Radial-velocity Data

Our full CARMENES data set for the VIS channel is presented in Table 5, along with the corresponding activity indicators at each epoch.

Table 5
Radial-velocity Measurements for the Star Along with Activity Indicators at Each Epoch

Name	BJD (−2,450,000)	RV (m s^{-1})	σ_{RV} (m s^{-1})	CRX (m s^{-1} Np^{-1})	dLW (10^3 m^2 s^{-2})	BIS (km s^{-1})	H_α (km s^{-1})	Ca II IRT a (km s^{-1})	Instrument	S/N
TOI-1759	9054.56851	2.33	2.51	49.44	1.48	−0.0774	0.074	0.0094	CARMENES-VIS	119.4
TOI-1759	9067.60481	3.32	2.32	43.58	−0.04	−0.0646	0.082	0.0128	CARMENES-VIS	97.6
TOI-1759	9068.57556	1.86	1.86	29.70	−11.16	−0.0776	0.074	0.0290	CARMENES-VIS	94.3
TOI-1759	9069.59957	0.86	1.78	21.57	−5.31	−0.0635	0.054	0.0154	CARMENES-VIS	101.8
TOI-1759	9070.55690	2.17	1.85	7.88	−5.34	−0.0764	0.076	0.0237	CARMENES-VIS	111.2
TOI-1759	9076.57116	6.20	2.55	15.86	−22.86	−0.0763	0.078	0.0304	CARMENES-VIS	80.6
TOI-1759	9078.60935	8.44	2.01	18.62	−11.90	−0.0719	0.068	0.0068	CARMENES-VIS	103.2
TOI-1759	9079.59579	3.59	2.33	36.88	−16.68	−0.0677	0.079	0.0154	CARMENES-VIS	104.2
TOI-1759	9081.58773	6.10	2.47	−16.45	−19.67	−0.0604	0.079	0.0099	CARMENES-VIS	81.8
TOI-1759	9084.55634	0.35	1.48	−10.41	2.25	−0.0560	0.093	0.0120	CARMENES-VIS	103.7
TOI-1759	9087.59796	1.37	2.12	6.67	−1.17	−0.0517	0.069	0.0071	CARMENES-VIS	104.8
TOI-1759	9089.53629	−1.43	1.95	−8.83	−5.14	−0.0600	0.071	0.0110	CARMENES-VIS	109.4
TOI-1759	9090.55842	−3.51	2.75	−8.03	−14.72	−0.0490	0.069	0.0033	CARMENES-VIS	76.3
TOI-1759	9091.54399	−8.08	3.58	−32.14	−6.07	−0.0609	0.049	0.0216	CARMENES-VIS	48.5
					…					
TOI-1759	9173.30701	−3.00	2.43	−12.31	12.00	−0.0291	0.052	0.0104	CARMENES-VIS	93.4
TOI-1759	9174.31626	−2.65	1.89	−11.97	15.74	−0.0118	0.065	−0.0023	CARMENES-VIS	90.7
TOI-1759	9175.35015	6.53	2.21	−32.46	7.19	−0.0132	0.102	0.0127	CARMENES-VIS	77.8
TOI-1759	9176.32926	−10.27	2.28	−14.38	20.12	−0.0227	0.064	0.0020	CARMENES-VIS	114.3
TOI-1759	9177.32923	−1.93	1.78	−35.19	13.28	−0.0312	0.066	0.0014	CARMENES-VIS	111.0
TOI-1759	9178.28239	−11.01	1.90	−15.77	7.78	−0.0338	0.086	0.0099	CARMENES-VIS	95.8
TOI-1759	9183.29700	−10.37	2.20	−31.60	−2.18	−0.0157	0.071	0.0123	CARMENES-VIS	97.3
TOI-1759	9186.33693	−9.05	4.74	−45.55	−22.24	−0.0773	0.037	0.0161	CARMENES-VIS	27.1
TOI-1759	9187.30129	−1.25	3.31	−45.82	−24.91	−0.0299	0.103	−0.0038	CARMENES-VIS	50.3
TOI-1759	9193.27483	4.02	3.18	0.08	−0.95	−0.0247	0.084	−0.0052	CARMENES-VIS	64.2
TOI-1759	9196.26135	−8.36	2.97	−9.94	7.30	−0.0186	0.032	−0.0079	CARMENES-VIS	72.1
TOI-1759	9197.34852	−4.98	3.64	−22.89	−3.08	−0.0198	0.085	0.0218	CARMENES-VIS	57.4
TOI-1759	9209.39053	6.56	6.36	7.17	−27.90	−0.0371	0.026	0.0052	CARMENES-VIS	25.7
TOI-1759	9216.25949	1.84	5.71	−48.81	3.21	−0.0156	0.125	0.0121	CARMENES-VIS	38.2
TOI-1759	9218.29595	−5.22	2.45	−15.32	−17.68	−0.0126	0.082	0.0091	CARMENES-VIS	61.6
TOI-1759	9219.28687	−4.05	3.34	−61.08	−22.66	−0.0350	0.055	0.0109	CARMENES-VIS	47.8
TOI-1759	9231.28008	1.00	2.57	−4.70	3.51	−0.0059	0.052	−0.0024	CARMENES-VIS	92.8
TOI-1759	9232.28137	2.54	2.77	−4.43	10.19	−0.0298	0.052	−0.0001	CARMENES-VIS	96.4

Note. Signal-to-noise ratio (S/N) for CARMENES-VIS data corresponds to the S/N at order 36 (at about 840 nm). A sample of the full radial-velocity data set and activity indicators is shown here. The entirety of this table is available in a machine-readable form in the online journal.

(This table is available in its entirety in machine-readable form.)

Appendix B
Photometric Data

Our full photometric data set targeting transits of TOI-1759 is presented in Table 6. The long-term photometry is presented in Table 7.

Table 6
Photometric Transits of the Planet

Name	BJD −2,450,000	Relative Flux	Error	Instrument	Standardized Airmass
TOI-1759	8738.65456	1.000458	0.001213	TESS—Sector 16	⋯
TOI-1759	8738.65594	0.999531	0.001211	TESS—Sector 16	⋯
TOI-1759	8738.65733	1.000397	0.001213	TESS—Sector 16	⋯
TOI-1759	8738.65872	1.001858	0.001212	TESS—Sector 16	⋯
TOI-1759	8738.66011	0.999702	0.001212	TESS—Sector 16	⋯
TOI-1759	8738.66150	0.999855	0.001212	TESS—Sector 16	⋯
TOI-1759	8738.66289	0.999816	0.001210	TESS—Sector 16	⋯
TOI-1759	8738.66428	0.999837	0.001209	TESS—Sector 16	⋯
TOI-1759	8738.66567	0.998040	0.001210	TESS—Sector 16	⋯
TOI-1759	8738.66706	0.998851	0.001212	TESS—Sector 16	⋯
TOI-1759	8738.66844	0.999615	0.001213	TESS—Sector 16	⋯
		⋯			
TOI-1759	8990.54955	0.995134	0.001107	Albanya-0.4 m (OAA-Ic)	−1.372
TOI-1759	8990.55022	1.000704	0.001110	Albanya-0.4 m (OAA-Ic)	−1.380
TOI-1759	8990.55090	0.998573	0.001110	Albanya-0.4 m (OAA-Ic)	−1.388
TOI-1759	8990.55159	0.997527	0.001110	Albanya-0.4 m (OAA-Ic)	−1.396
TOI-1759	8990.55225	0.999177	0.001110	Albanya-0.4 m (OAA-Ic)	−1.403
TOI-1759	8990.55293	1.001281	0.001110	Albanya-0.4 m (OAA-Ic)	−1.411
TOI-1759	8990.55360	0.998378	0.001107	Albanya-0.4 m (OAA-Ic)	−1.419
TOI-1759	8990.55428	0.998890	0.001113	Albanya-0.4 m (OAA-Ic)	−1.426
TOI-1759	8990.55496	0.998735	0.001113	Albanya-0.4 m (OAA-Ic)	−1.434
TOI-1759	8990.55563	0.997969	0.001113	Albanya-0.4 m (OAA-Ic)	−1.442

Note. The Standarized Airmass column corresponds to the airmass values subtracted by their mean and divided by their standard deviation. A sample of the full photometric data set is shown here. The entirety of this table is available in a machine-readable form in the online journal or the source file used to generate this compiled PDF version.

(This table is available in its entirety in machine-readable form.)

Table 7
Long-term Photometric Measurements of TOI-1759

Name	BJD −2,450,000	Relative Flux	Error	Instrument
TOI-1759	9010.61701	0.993732	0.000714	Joan-Oro-0.8 m (TJO)
TOI-1759	9010.61758	0.993128	0.000714	Joan-Oro-0.8 m (TJO)
TOI-1759	9010.61813	0.991751	0.000714	Joan-Oro-0.8 m (TJO)
TOI-1759	9010.61868	0.992962	0.000714	Joan-Oro-0.8 m (TJO)
TOI-1759	9010.61923	0.992559	0.000714	Joan-Oro-0.8 m (TJO)
TOI-1759	9010.61978	0.990158	0.000714	Joan-Oro-0.8 m (TJO)
TOI-1759	9010.62033	0.990918	0.000714	Joan-Oro-0.8 m (TJO)
TOI-1759	9010.62089	0.991625	0.000714	Joan-Oro-0.8 m (TJO)
TOI-1759	9010.62145	0.992897	0.000719	Joan-Oro-0.8 m (TJO)
TOI-1759	9010.62200	0.991557	0.000719	Joan-Oro-0.8 m (TJO)
TOI-1759	9010.62255	0.991023	0.000719	Joan-Oro-0.8 m (TJO)
		…		
TOI-1759	9457.65199	1.003121	0.001813	Sierra-Nevada-0.9 m (SNO-V)
TOI-1759	9457.65339	1.005637	0.001809	Sierra-Nevada-0.9 m (SNO-V)
TOI-1759	9457.65479	1.003229	0.001785	Sierra-Nevada-0.9 m (SNO-V)
TOI-1759	9457.65619	1.003976	0.001838	Sierra-Nevada-0.9 m (SNO-V)
TOI-1759	9457.65759	1.003824	0.001882	Sierra-Nevada-0.9 m (SNO-V)
TOI-1759	9457.65899	1.006960	0.001844	Sierra-Nevada-0.9 m (SNO-V)
TOI-1759	9457.66039	1.001677	0.001862	Sierra-Nevada-0.9 m (SNO-V)
TOI-1759	9457.66320	1.000984	0.001788	Sierra-Nevada-0.9 m (SNO-V)
TOI-1759	9457.66460	1.005191	0.001829	Sierra-Nevada-0.9 m (SNO-V)
TOI-1759	9457.66600	1.002202	0.001869	Sierra-Nevada-0.9 m (SNO-V)

Note. A sample of the full photometric data set is shown here. The entirety of this table is available in a machine-readable form in the online journal or the source file used to generate this compiled PDF version.

(This table is available in its entirety in machine-readable form.)

ORCID iDs

Néstor Espinoza https://orcid.org/0000-0001-9513-1449
Enric Pallé https://orcid.org/0000-0003-0987-1593
Jonas Kemmer https://orcid.org/0000-0003-3929-1442
Rafael Luque https://orcid.org/0000-0002-4671-2957
José A. Caballero https://orcid.org/0000-0002-7349-1387
Carlos Cifuentes https://orcid.org/0000-0003-1715-5087
Stephan Stock https://orcid.org/0000-0002-1166-9338
Karan Molaverdikhani https://orcid.org/0000-0002-0502-0428
Giuseppe Morello https://orcid.org/0000-0002-4262-5661
Diana Kossakowski https://orcid.org/0000-0002-0436-7833
Martin Schlecker https://orcid.org/0000-0001-8355-2107
Paz Bluhm https://orcid.org/0000-0002-0374-8466
Thomas Henning https://orcid.org/0000-0002-1493-300X
Laura Kreidberg https://orcid.org/0000-0003-0514-1147
Nicolas Lodieu https://orcid.org/0000-0002-3612-8968
Mahmoudreza Oshagh https://orcid.org/0000-0002-0715-8789
Sabine Reffert https://orcid.org/0000-0002-0460-8289
Ignasi Ribas https://orcid.org/0000-0002-6689-0312
Trifon Trifonov https://orcid.org/0000-0002-0236-775X
David Montes https://orcid.org/0000-0002-7779-238X
Grzegorz Nowak https://orcid.org/0000-0002-7031-7754
Mathias Zechmeister https://orcid.org/0000-0002-6532-4378
Karen A. Collins https://orcid.org/0000-0001-6588-9574
Steve B. Howell https://orcid.org/0000-0002-2532-2853
David R. Ciardi https://orcid.org/0000-0002-5741-3047
Rachel A. Matson https://orcid.org/0000-0001-7233-7508
Joshua E. Schlieder https://orcid.org/0000-0001-5347-7062
Thomas Barclay https://orcid.org/0000-0001-7139-2724
Tansu Daylan https://orcid.org/0000-0002-6939-9211
Diana Dragomir https://orcid.org/0000-0003-2313-467X
Joseph D. Twicken https://orcid.org/0000-0002-6778-7552
Joshua N. Winn https://orcid.org/0000-0002-4265-047X
David Latham https://orcid.org/0000-0001-9911-7388
George Ricker https://orcid.org/0000-0003-2058-6662

References

Aller, A., Lillo-Box, J., Jones, D., Miranda, L. F., & Barceló Forteza, S. 2020, A&A, 635, A128
Amado, P. J., Bauer, F. F., Rodríguez López, C., et al. 2021, A&A, 650, A188
Batalha, N. E., Mandell, A., Pontoppidan, K., et al. 2017, PASP, 129, 064501
Bayo, A., Rodrigo, C., Barrado Y Navascués, D., et al. 2008, A&A, 492, 277
Benneke, B., Wong, I., Piaulet, C., et al. 2019, ApJL, 887, L14
Borucki, W. J., Koch, D., Basri, G., et al. 2010, Sci, 327, 977
Burt, J. A., Dragomir, D., Mollière, P., et al. 2021, AJ, 162, 87
Caballero, J. A., Guàrdia, J., López del Fresno, M., et al. 2016, Proc. SPIE, 9910, 99100E
Ciardi, D. R., Beichman, C. A., Horch, E. P., & Howell, S. B. 2015, ApJ, 805, 16
Cifuentes, C., Caballero, J. A., Cortés-Contreras, M., et al. 2020, A&A, 642, A115
Cloutier, R., Astudillo-Defru, N., Bonfils, X., et al. 2019, A&A, 629, A111
Collins, K. A., Kielkopf, J. F., Stassun, K. G., & Hessman, F. V. 2017, AJ, 153, 77
Colomé, J., Francisco, X., Ribas, I., Casteels, K., & Martín, J. 2010, Proc. SPIE, 7740, 774009
Colome, J., & Ribas, I. 2006, IAUSS, 6, 11
Crossfield, I. J. M., & Kreidberg, L. 2017, AJ, 154, 261
Cutri, R. M., Wright, E. L., Conrow, T., et al. 2014, yCat, II, 328
Dittmann, J. A., Irwin, J. M., Charbonneau, D., et al. 2017, Natur, 544, 333
Dorn, C., Venturini, J., Khan, A., et al. 2017, A&A, 597, A37
Edwards, B., Changeat, Q., Mori, M., et al. 2021, AJ, 161, 44
Espinoza, N., & Jordán, A. 2016, MNRAS, 457, 3573
Espinoza, N., Kossakowski, D., & Brahm, R. 2019, MNRAS, 490, 2262

Foreman-Mackey, D., Agol, E., Angus, R., & Ambikasaran, S. 2017, AJ, 154, 220
Fraine, J., Deming, D., Benneke, B., et al. 2014, Natur, 513, 526
Fuhrmann, K. 1998, A&A, 338, 161
Fulton, B. J., & Petigura, E. A. 2018, AJ, 156, 264
Fulton, B. J., Petigura, E. A., Blunt, S., & Sinukoff, E. 2018, PASP, 130, 044504
Furlan, E., Ciardi, D. R., Everett, M. E., et al. 2017, AJ, 153, 71
Gaia Collaboration, Smart, R. L., Sarro, L. M., et al. 2021, A&A, 649, A6
Guerrero, N. M., Seager, S., Huang, C. X., et al. 2021, ApJS, 254, 39
Guo, X., Crossfield, I. J. M., Dragomir, D., et al. 2020, AJ, 159, 239
Gupta, A., & Schlichting, H. E. 2021, MNRAS, 504, 4634
Hippke, M., & Heller, R. 2019, A&A, 623, A39
Høg, E., Fabricius, C., Makarov, V. V., et al. 2000, A&A, 355, L27
Hsu, D. C., Ford, E. B., Ragozzine, D., & Ashby, K. 2019, AJ, 158, 109
Jenkins, J. M. 2002, ApJ, 575, 493
Jenkins, J. M., Chandrasekaran, H., McCauliff, S. D., et al. 2010, Proc. SPIE, 7740, 77400D
Jenkins, J. M., Twicken, J. D., McCauliff, S., et al. 2016, Proc. SPIE, 9913, 99133E
Kempton, E. M. R., Bean, J. L., Louie, D. R., et al. 2018, PASP, 130, 114401
Kipping, D. M. 2013, MNRAS, 435, 2152
Kite, E. S., Fegley, Bruce, J., Schaefer, L., & Ford, E. B. 2019, ApJL, 887, L33
Kostov, V. B., Schlieder, J. E., Barclay, T., et al. 2019, AJ, 158, 32
Kreidberg, L. 2015, PASP, 127, 1161
Kreidberg, L., Bean, J. L., Désert, J.-M., et al. 2014, Natur, 505, 69
Lafarga, M., Ribas, I., Lovis, C., et al. 2020, A&A, 636, A36
Leleu, A., Alibert, Y., Hara, N. C., et al. 2021, A&A, 649, A26
Lépine, S., Hilton, E. J., Mann, A. W., et al. 2013, AJ, 145, 102
Li, J., Tenenbaum, P., Twicken, J. D., et al. 2019, PASP, 131, 024506
Ma, Q., & Ghosh, S. K. 2021, MNRAS, 505, 3853
Marfil, E., Tabernero, H. M., Montes, D., et al. 2021, A&A, 656, A162
Matson, R. A., Howell, S. B., & Ciardi, D. R. 2019, AJ, 157, 211
Meadows, V. S., & Barnes, R. K. 2018, in Factors Affecting Exoplanet Habitability, ed. H. J. Deeg & J. A. Belmonte (Berlin: Springer), 57
Ment, K., Dittmann, J. A., Astudillo-Defru, N., et al. 2019, AJ, 157, 32
Molaverdikhani, K., Helling, C., Lew, B. W., et al. 2020a, A&A, 635, A31
Molaverdikhani, K., Henning, T., & Mollière, P. 2019, ApJ, 883, 194
Molaverdikhani, K., Henning, T., & Mollière, P. 2020b, ApJ, 899, 53
Mollière, P., Stolker, T., Lacour, S., et al. 2020, A&A, 640, A131
Mollière, P., Wardenier, J., van Boekel, R., et al. 2019, A&A, 627, A67
Morales, J. C., Mustill, A. J., Ribas, I., et al. 2019, Sci, 365, 1441
Morello, G., Zingales, T., Martin-Lagarde, M., Gastaud, R., & Lagage, P.-O. 2021, AJ, 161, 174
NASA Exoplanet Science Institute 2020, Planetary Systems Table https://catcopy.ipac.caltech.edu/dois/doi.php?id=10.26133/NEA12
Neil, A. R., & Rogers, L. A. 2020, ApJ, 891, 12
Passegger, V. M., Schweitzer, A., Shulyak, D., et al. 2019, A&A, 627, A161
Pidhorodetska, D., Moran, S. E., Schwieterman, E. W., et al. 2021, AJ, 162, 169
Quirrenbach, A., Amado, P. J., Caballero, J. A., et al. 2014, Proc. SPIE, 9147, 91471F
Quirrenbach, A., Amado, P. J., Ribas, I., et al. 2018, Proc. SPIE, 10702, 107020W
Ricker, G. R., Winn, J. N., Vanderspek, R., et al. 2015, JATIS, 1, 014003
Schlichting, H. E., & Young, E. D. 2021, arXiv:2107.10405
Schlieder, J. E., Gonzales, E. J., Ciardi, D. R., et al. 2021, FrASS, 8, 63
Schöfer, P., Jeffers, S. V., Reiners, A., et al. 2019, A&A, 623, A44
Schweitzer, A., Passegger, V. M., Cifuentes, C., et al. 2019, A&A, 625, A68
Scott, N. J., & Howell, S. B. 2018, Proc. SPIE, 10701, 107010G
Seager, S., Petkowski, J. J., Günther, M. N., et al. 2021, Univ, 7, 172
Skrutskie, M. F., Cutri, R. M., Stiening, R., et al. 2006, AJ, 131, 1163
Smith, J. C., Stumpe, M. C., Van Cleve, J. E., et al. 2012, PASP, 124, 1000
Speagle, J. S. 2020, MNRAS, 493, 3132
Stassun, K. G., Oelkers, R. J., Paegert, M., et al. 2019, AJ, 158, 138
Stock, S., Kemmer, J., Reffert, S., et al. 2020a, A&A, 636, A119
Stock, S., Nagel, E., Kemmer, J., et al. 2020b, A&A, 643, A112
Stumpe, M. C., Smith, J. C., Catanzarite, J. H., et al. 2014, PASP, 126, 100
Stumpe, M. C., Smith, J. C., Van Cleve, J. E., et al. 2012, PASP, 124, 985
Tasker, E., Tan, J., Heng, K., et al. 2017, NatAs, 1, 0042
Trifonov, T., Lee, M. H., Kürster, M., et al. 2020, A&A, 638, A16
Trotta, R. 2008, ConPh, 49, 71
Tsiaras, A., Waldmann, I. P., Tinetti, G., Tennyson, J., & Yurchenko, S. N. 2019, NatAs, 3, 1086
Twicken, J. D., Catanzarite, J. H., Clarke, B. D., et al. 2018, PASP, 130, 064502
Wizinowich, P., Acton, D. S., Shelton, C., et al. 2000, PASP, 112, 315
Yu, X., He, C., Zhang, X., et al. 2021, NatAs, 5, 822
Zechmeister, M., & Kürster, M. 2009, A&A, 496, 577
Zechmeister, M., Reiners, A., Amado, P. J., et al. 2018, A&A, 609, A12
Zeng, L., Jacobsen, S. B., Sasselov, D. D., et al. 2019, PNAS, 116, 9723
Zeng, L., Sasselov, D. D., & Jacobsen, S. B. 2016, ApJ, 819, 127